nature geoscience
ARTICLES
https://doi.org/10.1038/s41561-019-0436-1

Field-experiment constraints on the enhancement of the terrestrial carbon sink by CO_2 fertilization

Yongwen **Liu**[1,2], Shilong **Piao**[1,2,3*], Thomas **Gasser**[4], Philippe **Ciais**[5], Hui **Yang**[3], Han **Wang**[6], Trevor F. **Keenan**[7,8], Mengtian **Huang**[3], Shiqiang **Wan**[9], Jian **Song**[9], Kai **Wang**[3], Ivan A. **Janssens**[10], Josep **Peñuelas**[11,12], Chris **Huntingford**[13], Xuhui **Wang**[3], Muhammad **Altaf Arain**[14], Yuanyuan **Fang**[15], Joshua B. **Fisher**[16], Maoyi **Huang**[17], Deborah N. **Huntzinger**[18], Akihiko **Ito**[19], Atul **Jain**[20], Jiafu **Mao**[21], Anna M. **Michalak**[15], Changhui **Peng**[22,23], Benjamin **Poulter**[24], Christopher **Schwalm**[25,26], Xiaoying **Shi**[21], Hanqin **Tian**[27], Yaxing **Wei**[21], Ning **Zeng**[28], Qiuan **Zhu**[29] and Tao **Wang**[1,2]

Clarifying how increased atmospheric CO_2 concentration (eCO_2) contributes to accelerated land carbon sequestration remains important since this process is the largest negative feedback in the coupled carbon–climate system. Here, we constrain the sensitivity of the terrestrial carbon sink to eCO_2 over the temperate Northern Hemisphere for the past five decades, using 12 terrestrial ecosystem models and data from seven CO_2 enrichment experiments. This constraint uses the heuristic finding that the northern temperate carbon sink sensitivity to eCO_2 is linearly related to the site-scale sensitivity across the models. The emerging data-constrained eCO_2 sensitivity is 0.64 ± 0.28 PgC yr^{-1} per hundred ppm of eCO_2. Extrapolating worldwide, this northern temperate sensitivity projects the global terrestrial carbon sink to increase by 3.5 ± 1.9 PgC yr^{-1} for an increase in CO_2 of 100 ppm. This value suggests that CO_2 fertilization alone explains most of the observed increase in global land carbon sink since the 1960s. More CO_2 enrichment experiments, particularly in boreal, arctic and tropical ecosystems, are required to explain further the responsible processes.

Human activities have profoundly altered the global carbon cycle[1]. About 600 PgC was emitted as CO_2 to the atmosphere during 1750–2015 due to the burning of fossil fuel, cement production and land-use change[2]. It is estimated that terrestrial ecosystems responded to this perturbation by absorbing about 32% of the cumulative anthropogenic emissions[2] and therefore played a key role in mitigating climate change[3–5]. The terrestrial CO_2 sink (excluding emissions from land-use change) estimate doubled between the 1960s (period 1960–1969) and the current decade (2007–2016)[2] (Fig. 1a). Terrestrial ecosystem model simulations have indicated that increasing CO_2 (eCO_2) is the main driver of the increase in the terrestrial carbon sink[5–8]. However, the magnitude of this eCO_2 fertilization differs strongly between models (Fig. 1b). Reducing this uncertainty is critical for refining understanding of the role of land in the future evolution of the coupled terrestrial carbon cycle/climate system, one of the Grand Challenges acknowledged by the World Climate Research Programme[9].

Free-air CO_2-enrichment (FACE) experiments have been conducted at the ecosystem scale since the 1980s to measure the response of carbon fluxes and stocks to eCO_2 (ref. 10). These comprehensive experiments and data sets provide insights into local nutrient limitations and physiological mechanisms controlling the effect of eCO_2 on net primary productivity (NPP) and ecosystem carbon storage[10,11]. However, the implications of their findings have not been scaled up to estimate large-scale effects of eCO_2 on carbon sinks. Overall, meta-analyses of FACE experiment results find

---

[1]Key Laboratory of Alpine Ecology, Institute of Tibetan Plateau Research, Chinese Academy of Sciences, Beijing, China. [2]CAS Center for Excellence in Tibetan Plateau Earth Sciences, Chinese Academy of Sciences, Beijing, China. [3]Sino-French Institute for Earth System Science, College of Urban and Environmental Sciences, Peking University, Beijing, China. [4]International Institute for Applied Systems Analysis (IIASA), Laxenburg, Austria. [5]Laboratoire des Sciences du Climat et de l'Environnement, CEA-CNRS-UVSQ, Gif-sur-Yvette, France. [6]Department of Earth System Science, Tsinghua University, Beijing, China. [7]Climate and Ecosystem Sciences Division, Lawrence Berkeley National Laboratory, Berkeley, CA, USA. [8]Department of Environmental Science, Policy and Management, UC Berkeley, Berkeley, CA, USA. [9]College of Life Sciences, Hebei University, Baoding, Hebei, China. [10]Department of Biology, University of Antwerp, Wilrijk, Belgium. [11]CREAF, Cerdanyola del Valles, Barcelona, Catalonia, Spain. [12]CSIC, Global Ecology Unit CREAF-CSIC-UAB, Bellaterra, Barcelona, Catalonia, Spain. [13]Centre for Ecology and Hydrology, Wallingford, UK. [14]School of Geography and Earth Sciences and McMaster Centre for Climate Change, McMaster University, Hamilton, ON, Canada. [15]Department of Global Ecology, Carnegie Institution for Science, Stanford, CA, USA. [16]Jet Propulsion Laboratory, California Institute of Technology, Pasadena, CA, USA. [17]Atmospheric Sciences and Global Change Division, Pacific Northwest National Laboratory, Richland, WA, USA. [18]School of Earth Sciences and Environmental Sustainability, Northern Arizona University, Flagstaff, AZ, USA. [19]National Institute for Environmental Studies, Tsukuba, Japan. [20]Department of Atmospheric Sciences, University of Illinois at Urbana-Champaign, Urbana, IL, USA. [21]Environmental Sciences Division and Climate Change Science Institute, Oak Ridge National Laboratory, Oak Ridge, TN, USA. [22]Department of Biology Sciences, Institute of Environment Sciences, University of Quebec at Montreal, Montreal, Canada. [23]Laboratory for Ecological Forecasting and Global Change, College of Forestry, Northwest A&F University, Yangling, Shaanxi, China. [24]NASA GSFC, Biospheric Sciences Lab., Greenbelt, MD, USA. [25]Woods Hole Research Center, Falmouth, MA, USA. [26]Center for Ecosystem Science and Society, Northern Arizona University, Flagstaff, AZ, USA. [27]International Center for Climate and Global Change Research and School of Forestry and Wildlife Sciences, Auburn University, Auburn, AL, USA. [28]Department of Atmospheric and Oceanic Science, University of Maryland, College Park, MD, USA. [29]State Key Laboratory of Soil Erosion and Dryland Farming on the Loess Plateau, Northwest A&F University, Yangling, China. *e-mail: slpiao@pku.edu.cn

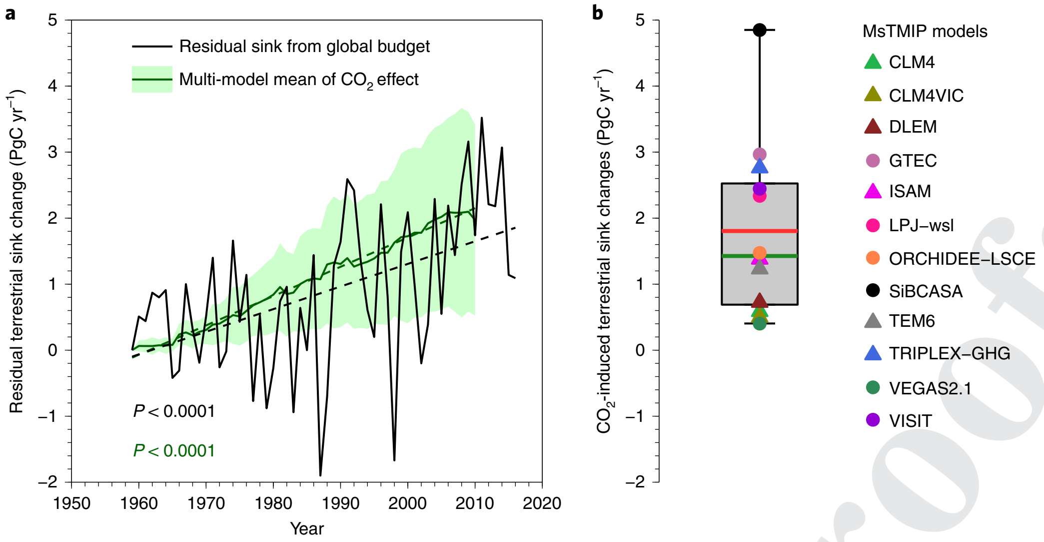

Fig. 1 | Effect of eCO$_2$ on the change in the global residual terrestrial sink during the past five decades. **a**, Changes in the residual terrestrial sink (excluding emissions from land-use changes) from global budget[2] and the effect of eCO$_2$ on the residual terrestrial sink changes from 12 MsTMIP models (shown as multi-model mean ± s.d., shaded green area) relative to 1959. The dashed lines indicate unconstrained linear regressions. **b**, The eCO$_2$-induced change in global residual terrestrial sink during 1960s (1960–1969) and 2000s (2000–2009) in the MsTMIP models. The grey rectangle spans the first to the third quartiles. The red and green segments inside the rectangle indicate the mean and median, respectively. The whiskers above and below the rectangle indicate the maximum and minimum, respectively. The triangles indicate the models with dynamic nitrogen cycles.

that eCO$_2$ generally stimulates plant growth and increases ecosystem carbon storage[12,13]. The FACE experiments have been mainly in temperate ecosystems and generally lasted for only a few years[10]. The effects of eCO$_2$ differ with environmental conditions and local biotic factors[14]. They also change over the duration of experiments, in relation to the ability of plants to take up more nutrients[15], for example by increased below-ground allocation to roots[16] and mycorhizae symbiosis[17]. New approaches are needed to link these effects, which are implicit in the FACE experiments, to large-scale model simulations of the CO$_2$ fertilization effect on the terrestrial carbon sink.

We quantify the sensitivity of terrestrial CO$_2$ sink to eCO$_2$ (parameter B) in the Northern Hemisphere temperate zone (23–50° N) by combining the results of terrestrial ecosystem models with FACE experiments using an emergent-constraint approach[18] (Methods). Emergent-constraint approaches have been successfully applied to constrain the effects of climatic warming on tropical carbon storage[18], the sensitivity of gross primary productivity (GPP) to eCO$_2$ (ref. [19]), the projections of future global carbon sinks[20], the sensitivity of global rice yield to long-term climate change[21] and the ratio of plant transpiration to land evapotranspiration[22]. We use the output of 12 terrestrial models from the Multi-scale Synthesis and Terrestrial Model Intercomparison Project (MsTMIP)[23] (Supplementary Table 1) and the observed site-scale sensitivity of the net ecosystem production (NEP) to eCO$_2$ (Methods) from seven FACE experiments. All seven FACE experiments have a duration longer than one growing season (Supplementary Tables 2 and 3). They additionally include both N-limited and N-rich sites and both arbuscular-mycorrhizae- and ectomycorrhizae-dominated ecosystems. The emergent constraint used here is a heuristic relationship between modelled B at different spatial scales. That is, it links the sensitivity B_{NH} for all northern temperate ecosystems and the modelled mean sensitivity from the experiment site locations, B_{Site} (Methods). This relationship can then be used with FACE data-based knowledge of B_{Site} to constrain the value of B_{NH}.

Comparison of observed and modelled sensitivities

The FACE experimental configuration is the introduction of a step increase of atmospheric CO$_2$. After this, NPP generally increases, but this stimulation often slows down after a few years, which many attribute to nutrient limitations (for example, Norby et al.[24]). Following the initial step increase of NPP, heterotrophic respiration (HR) also increases. This lag between HR and NPP leads to a transient sink (NEP), which integrates the direct effects of eCO$_2$ on NPP and delayed effects on respiration. The latter is a function of carbon allocation[25] and the turnover times of excess carbon in biomass, litter and soil organic matter. By contrast, in the historical simulations of the global models, the forcing of atmospheric CO$_2$ on different terrestrial components can be isolated through separate factorial simulations. However, in those simulations, CO$_2$ does not increase abruptly but follows the historical atmospheric trend (roughly corresponding to an increase of 1.4 ppm yr^{-1} for 1959–2010). In response to such a gradual increase of CO$_2$, NPP simulated by models increases slowly, and HR follows this increase with a lag. The resulting historical response of NEP to eCO$_2$ in models is thus not directly comparable to the short-term response to a step change in the FACE experiments. To link the two responses (FACE-based short-term step increase of CO$_2$ versus land model–based gradual rise of CO$_2$), we develop substitute pulse–response models (Methods). These can infer the step-response of NEP to eCO$_2$ in each MsTMIP model to mimic the conditions of the FACE experiment sites (Supplementary Fig. 1). The parameters of substitute models are the NPP sensitivity to eCO$_2$ and the turnover of excess carbon in total biomass and soil carbon pools. As an initial test, the substitute models generally emulate successfully the eCO$_2$-induced historical total biomass and soil carbon evolution from the original complex process-oriented MsTMIP models (generally $R^2 > 0.95$, $P < 0.0001$, Supplementary Figs. 2–13). Nevertheless, the substitute models do not work well to reproduce the biomass carbon pool evolution at grassland sites for 5 of 12 MsTMIP models (5 models at Duolun and 3 models at PHACE), particularly when NPP monotonically increases but biomass carbon pool suddenly declines (Supplementary Figs. 2, 5, 7–9). This, therefore, may further result in uncertainty in the estimates of both Northern Hemisphere temperate and global terrestrial B.

A second issue needs to be addressed to enable comparison of MsTMIP estimates with FACE data. Atmospheric CO$_2$ was increased abruptly at the FACE sites from recent amounts (~381 ppm) to about twice pre-industrial CO_2 levels. That is a step increase (ΔCO_2) of about 200 ppm (Supplementary Table 2). However, ΔCO_2 at FACE sites is significantly larger than ΔCO_2 in models during the recent historical period (that is, about 60 ppm between 1959–1968 and 2001–2010). Because the response of photosynthesis to eCO_2 is nonlinear and convex[26], we extrapolate the observed FACE-based NEP sensitivity to $\Delta CO_2 = 200$ ppm to $\Delta CO_2 = 60$ ppm on a background of 320 ppm as observed during the past 50 years. This is performed using (1) a theoretical model of photosynthesis (Pmodel), which is extensively supported by eddy-covariance measurements of CO_2 exchange and FACE observations[27], and (2) a logarithmic function of photosynthetic response to eCO_2 (refs. [3,28]). These algorithms provide us with observation-based estimates of B_{Site} consistent with historical CO_2 levels, that is, $B_{\mathrm{Site}}^{\mathrm{Hist}}$ (Methods). Nevertheless, such scaling is based on theoretical response curves of photosynthesis to CO_2 and thus subject to an unknown level of uncertainty due to incomplete knowledge on acclimation and the shape of the true response of ecosystem photosynthesis to eCO_2.

Northern Hemisphere temperate terrestrial *B* constrained by FACE observations

The sensitivity of the Northern Hemisphere temperate ecosystems carbon sink to yearly changing CO_2, $B_{\mathrm{NH}}^{\mathrm{Mod}}$ corresponding to the period 1959–2010, is found to be linearly correlated across the 12 terrestrial ecosystem models, with the modelled short-term response to a CO_2 step-increase (of 60 ppm) at each FACE location ($R^2 = 0.86$, $P < 0.0001$; Fig. 2a). The latter is diagnosed from the emulator of each model, as outlined above. Critically, this emergent constraint result indicates that a correspondence can be found between expected response to slowing changing CO_2 levels and a step change. That is, models with a large step-response to an abrupt increase in CO_2 at site-scale generally also produce a large $B_{\mathrm{NH}}^{\mathrm{Mod}}$. The linear emergent relationship across the models in Fig. 2a therefore provides a mechanism to constrain the impact of eCO_2 on Northern Hemisphere temperate ecosystems' NEP using the sensitivities inferred from FACE experiments, $B_{\mathrm{Site}}^{\mathrm{Hist}} = 75 \pm 28\,\mathrm{g\,C\,m^{-2}\,yr^{-1}}$ [100 ppm]$^{-1}$ (mean ± s.d., indicated by the light grey area in Fig. 2a). This $B_{\mathrm{Site}}^{\mathrm{Hist}}$ quantity is extrapolation of FACE observations to smaller jumps in CO_2 ($\Delta CO_2 = 60$ ppm) added to a background value of 320 ppm on the basis of the Pmodel[27], again as outlined above.

The relationship shown in Fig. 2a produces a probability density function (PDF) of $B_{\mathrm{NH}}^{\mathrm{Mod}}$ constrained by the eCO_2 experiment-based PDF of $B_{\mathrm{Site}}^{\mathrm{Hist}}$ (Fig. 2b). The unconstrained $B_{\mathrm{NH}}^{\mathrm{Mod}}$ of 0.58 ± 0.33 PgC yr^{-1} [100 ppm]$^{-1}$ (mean ± s.d.) is found to be lower than the observation-constrained value of 0.64 ± 0.28 PgC yr^{-1} [100 ppm]$^{-1}$ (indicated by the light red area in Fig. 2a). Multiplying the constrained B_{NH} by the historical increase in atmospheric CO_2 (57 ppm) provides an estimate of the historical CO_2 fertilization to the Northern Hemisphere terrestrial carbon sink as 0.36 ± 0.16 PgC yr^{-1} between the 1960s (1960–1969) and the 2000s (2000–2009). Despite the small quantity of FACE data, our estimate of constrained B_{NH} is robust when calculated using six, five and four eCO_2 experiment sites separately (Supplementary Fig. 14). The constrained B_{NH} is also robust using either the Pmodel (Methods equation [5])[27] at FACE sites or the alternative logarithmic function for the non-linear response of photosynthesis to CO_2 (Methods equation [14])[3,28] with all other conditions unchanged (Supplementary Fig. 15 and Methods).

Six of the twelve MsTMIP models incorporated processes controlling carbon–nitrogen (C–N) interactions (Supplementary Table 1), so we constrained B_{NH} values from carbon-only models and from C–N models separately. The Northern Hemisphere temperate ecosystems and site-level *B* are correlated for both the carbon-only models ($R^2 = 0.90$, $P = 0.004$; Fig. 2c) and the C–N models ($R^2 = 0.82$, $P = 0.013$; Fig. 2e). The constrained value of B_{NH} is 0.67 ± 0.24 PgC yr^{-1} [100 ppm]$^{-1}$ for the carbon-only models (Fig. 2c,d) and 0.71 ± 0.39 PgC yr^{-1} [100 ppm]$^{-1}$ for the C–N models (Fig. 2e,f); thus, we find no significant difference of constrained sensitivity depending on whether N cycling is included in models. Nevertheless, the slope of the linear relationship between B_{NH} and B_{Site} across the C–N models (slope = 0.013; Fig. 2e) is higher than that across the carbon-only models (slope = 0.008; Fig. 2c). This indicates that the emergent relationship across models can change when most models consider a new process, such as here for the N cycle. The relationship may be refined further when, for example, models routinely model the phosphorus cycle[29]. In addition, the temperate sites in our study mainly reflect forest ecosystems, with only two grassland sites and no site in shrublands or other ecosystems. Therefore, the relationship between Northern Hemisphere temperate ecosystems and site-level *B* across models, and the data-constrained BNH value, may adjust when new FACE sites become available and are included.

Compared to the constrained B_{NH} from the 12 models (0.64 ± 0.28 PgC yr^{-1} [100 ppm]$^{-1}$), B_{NH} is slightly overestimated by carbon-only models (0.74 ± 0.33 PgC yr^{-1} [100 ppm]$^{-1}$), but is generally underestimated by C–N models (0.41 ± 0.26 PgC yr^{-1} [100 ppm]$^{-1}$) (Supplementary Table 4). Specifically, for the C–N models, the observation-constrained B_{NH} is comparable with three of the six C–N models (ISAM, TEM6 and TRIPLEX-GHG) but is underestimated by the others (CLM4, CLMVIC and DLEM) (Fig. 2a). This is consistent with the site-scale comparison between the observed and the modelled NEP sensitivity to eCO_2 ($B_{\mathrm{Site}}^{\mathrm{Hist}}$ and $B_{\mathrm{Site}}^{\mathrm{Mod}}$, Fig. 2a, Supplementary Fig. 16). In FACE experiments, N limitation regulated the eCO_2-induced increase in NPP at the Oak Ridge forest[24] and at the moderately fertile Duke forest[30] and in decade-long eCO_2-stimulation on plant biomass in a temperate grassland[31]. A large influence of mycorrhizal association across sites regulated the biomass increase in response to eCO_2 through mycorrhizal-N uptake[17]. The observed plant N uptake increase by eCO_2 is generally underestimated by C–N models at Duke-FACE and ORNL-FACE sites[11], but the eCO_2 effects on plant N uptake remain fully characterized in the other experiments used in this study. The evaluation of N limitation on B_{NH} in the C–N models in this study must be considered with caution because we do not know whether our set of eCO_2 experiments is representative of the real-world extent of N limitation in northern temperate ecosystems due to the limited number of eCO_2 experiments. Nevertheless, there is the suggestion that some models may have an overly strong N response.

Global terrestrial *B* constrained by FACE observations

We can also expand our findings to the global scale. Across the models, B_{NH} was linearly correlated with the sensitivity of the global terrestrial carbon sink to eCO_2, B_{Globe} ($R^2 = 0.79$, $P = 0.0001$; Fig. 2g). This means that models with a large B_{NH} also simulate a large B_{Globe}. Using the linear relationship between temperate B_{Site} and B_{Globe} across models, we estimated a constrained value for B_{Globe} of 3.5 ± 1.9 PgC yr^{-1} [100 ppm]$^{-1}$ (Supplementary Fig. 17a,b and Methods), similar to carbon-only and C–N models (Supplementary Fig. 17c–f). The simple yet powerful emerging relationship in the MsTMIP model ensemble between temperate and global ecosystem responses to eCO_2 does have caveats. It may be due to terrestrial ecosystem models having similar structures and thus possibly common biases spatially coherent over the globe. For example, they do not include specific response processes that could limit the NEP response to CO_2 in tropical ecosystems, such as phosphorus limitation[29], and do not distinguish between the responses of arbuscular-mycorrhizae- and ectomycorrhizae-dominated ecosystems, which was recently found to be a first-order explanation of increased biomass under eCO_2 (ref. [17]). The biases in modelling the eCO_2 effect across spatial scales (from site to globe) cannot be verified by FACE experiments only, due to the lack of FACE-based *B* data in boreal and tropical ecosystems. The planned extension of FACE experiments in tropical (for example, AmazonFACE) and boreal (for example, SwedFACE)

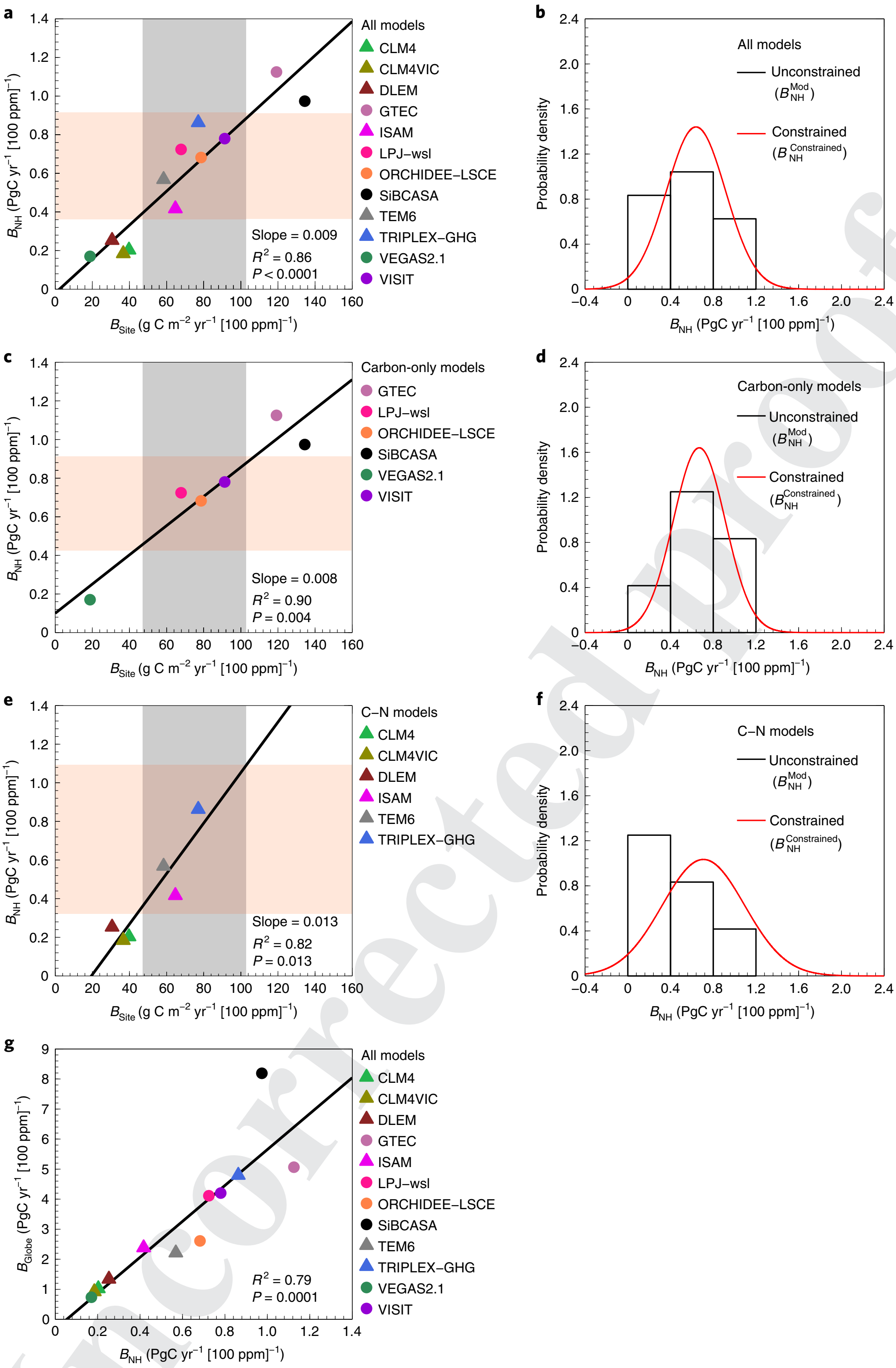

Fig. 2 | Emergent constraints on the sensitivity of the Northern Hemisphere temperate terrestrial carbon sink to eCO$_2$. a, Relationship between the Northern Hemisphere temperate zone and the site-scale responses of the terrestrial carbon sink to eCO$_2$ (B_{NH} and B_{Site}) for 1959–2010 across the MsTMIP models. B_{Site} is based on MsTMIP model simulation to be appropriate for a jump from 320 ppm to 380 ppm and extrapolation of FACE experiments also to a jump from 320 ppm to 380 ppm. The light grey area shows the observed B_{Site} in the FACE experiments (B_{Site}^{Hist}, shown as mean ± s.d.). The light red area shows FACE data-constrained B_{NH} ($B_{NH}^{Constrained}$, shown as mean ± s.d.). **b**, PDF for B_{NH}. The histogram indicates the PDF of unconstrained B_{NH} in the MsTMIP models (B_{NH}^{Mod}), assuming they are Gaussian distributed. The red line indicates the PDF of $B_{NH}^{Constrained}$. **c**, **d**, Same as **a** and **b** but using the carbon-only models. **e**, **f**, Same as **a** and **b** but using only the C–N models. **g**, Relationship between the Northern Hemisphere temperate zone and global responses of the terrestrial carbon sink to eCO$_2$ (B_{NH} and B_{Globe}) for 1959–2010 across the MsTMIP models. In **a**, **c**, **e** and **g**, the solid lines indicate unconstrained linear regressions and the triangles indicate the models with dynamic nitrogen cycles.

ecosystems[32], particularly designed with a gradual rise of CO_2 (ref. [33]), will improve the understanding of the mechanisms underlying the terrestrial carbon sink responses to eCO_2 away from mid-latitudes. Such additional FACE experiments would confirm or disconfirm our model-based extrapolation to estimate the global fertilization effect.

Combining the constrained B_{Globe} from the 12 models with the historical increase in atmospheric CO_2 (57 ppm) estimates the increased contribution of CO_2 fertilization to the global terrestrial carbon sink of $2.01 \pm 1.06\,\mathrm{PgC\,yr^{-1}}$ between the 1960s and the 2000s (Supplementary Fig. 18). This constrained value is comparable with the multi-model-mean of the carbon-only models but is underestimated by three of six C–N models (Supplementary Fig. 18). Subtracting the estimated eCO_2 effect and multi-model-mean of N deposition effect ($0.23 \pm 0.14\,\mathrm{PgC\,yr^{-1}}$) (Supplementary Fig. 19) from the observed residual land sink since 1960s ($1.2\,\mathrm{PgC\,yr^{-1}}$)[2], the effect of long-term warming (~0.9 °C) on the residual land sink between the 1960s and the 2000s is roughly estimated as $-1.04\,\mathrm{PgC\,yr^{-1}}$. This indicates a temperature sensitivity of NEP of $\Gamma_{\mathrm{Long}} = -1.16\,\mathrm{PgC\,yr^{-1}\,K^{-1}}$. This value falls within the range of the Global Carbon Budget data-constrained Γ_{Long} ($-1.57 \pm 0.51\,\mathrm{PgC\,yr^{-1}\,K^{-1}}$) on the basis of the linear relationship between long-term and interannual temperature sensitivities of the land net carbon sink across MsTMIP models (Supplementary Fig. 20 and Methods). Hence, the findings from the 'top-down' closure of the global carbon cycle[2] are comparable with our FACE-based 'bottom-up' emergent constraint value for B_{Globe} of $3.5 \pm 1.9\,\mathrm{PgC\,yr^{-1}\,[100\,ppm]^{-1}}$.

In summary, our results provide a constrained estimate of the sensitivity of the terrestrial carbon sink to eCO_2 for a transient climate responding to anthropogenic forcing. This is inferred by combining pulse–response functions implicit in terrestrial carbon-cycle models with FACE experiment observations, which can then be scaled to the CO_2 increase observed during the past five decades. We find a robust emergent constraint between these model estimates, mimicking FACE conditions via our inferred pulse-response of models, and their estimates of evolving temperate ecosystems NEP response to rising atmospheric CO_2 concentrations due to fossil-fuel burning. This allows us to extrapolate the direct FACE measurements to estimate an Northern Hemisphere temperate ecosystems NEP fertilization response of $0.64 \pm 0.28\,\mathrm{PgC\,yr^{-1}\,[100\,ppm]^{-1}}$ for the evolving conditions over recent decades. The consistency between model temperate regions and elsewhere allows us to make a unique data-based constraint on global vegetation direct physiological NEP response to rising CO_2 concentrations of $3.5 \pm 1.9\,\mathrm{PgC\,yr^{-1}\,[100\,ppm]^{-1}}$. Further verification is required, potentially through longer-term FACE experiments. These FACE experiments would enable a more comprehensive investigation of slowly evolving processes such as vegetation and soil carbon turnover rates, including their relationship to nutrients that may change for long-term eCO_2 exposure. To clarify the mechanisms underlying elevated CO_2 effects on terrestrial NEP, continued collaboration between experimentalists and modellers, for example, the FACE Model–Data Synthesis project[32,34], remains necessary.

Online content

Any methods, additional references, Nature Research reporting summaries, source data, statements of code and data availability and associated accession codes are available at https://doi.org/10.1038/s41561-019-0436-1.

Received: 16 August 2018; Accepted: 24 July 2019;
[redacted]

References

1. Field, C. B. & Raupach, M. R. *The Global Carbon Cycle: Integrating Humans, Climate, and the Natural World* (Island Press, 2004).
2. Le Quéré, C. et al. Global Carbon Budget 2017. *Earth Syst. Sci. Data* **10**, 405–448 (2018).
3. Friedlingstein, P. et al. On the contribution of CO_2 fertilization to the missing biospheric sink. *Glob. Biogeochem. Cycles* **9**, 541–556 (1995).
4. Shevliakova, E. et al. Historical warming reduced due to enhanced land carbon uptake. *Proc. Natl. Acad. Sci. USA* **110**, 16730–16735 (2013).
5. Schimel, D., Stephens, B. B. & Fisher, J. B. Effect of increasing CO_2 on the terrestrial carbon cycle. *Proc. Natl. Acad. Sci. USA* **112**, 436–441 (2015).
6. Huntzinger, D. N. et al. Uncertainty in the response of terrestrial carbon sink to environmental drivers undermines carbon–climate feedback predictions. *Sci. Rep.* **7**, 4765 (2017).
7. Keenan, T. F. et al. Recent pause in the growth rate of atmospheric CO_2 due to enhanced terrestrial carbon uptake. *Nat. Commun.* **7**, 13428 (2016).
8. Sitch, S. et al. Recent trends and drivers of regional sources and sinks of carbon dioxide. *Biogeosciences* **12**, 653–679 (2015).
9. Ilyina, T. & Friedlingstein, P. in *37th Session of the WCRP Joint Scientific Committee* (Geneva, Switzerland, 2016).
10. Norby, R. J. & Zak, D. R. Ecological lessons from free-air CO_2 enrichment (FACE) experiments. *Annu. Rev. Ecol. Evol. Syst.* **42**, 181–203 (2011).
11. Zaehle, S. et al. Evaluation of 11 terrestrial carbon–nitrogen cycle models against observations from two temperate free-air CO_2 enrichment studies. *New Phytol.* **202**, 803–822 (2014).
12. Jastrow, J. D. et al. Elevated atmospheric carbon dioxide increases soil carbon. *Glob. Change Biol.* **11**, 2057–2064 (2005).
13. De Graaff, M. A., van Groenigen, K. J., Six, J., Hungate, B. & van Kessel, C. Interactions between plant growth and soil nutrient cycling under elevated CO_2: a meta-analysis. *Glob. Change Biol.* **12**, 2077–2091 (2006).
14. Hickler, T. et al. CO_2 fertilization in temperate FACE experiments not representative of boreal and tropical forests. *Glob. Change Biol.* **14**, 1531–1542 (2008).
15. Finzi, A. C. et al. Increases in nitrogen uptake rather than nitrogen-use efficiency support higher rates of temperate forest productivity under elevated CO_2. *Proc. Natl. Acad. Sci. USA* **104**, 14014–14019 (2007).
16. Drake, J. E. et al. Increases in the flux of carbon belowground stimulate nitrogen uptake and sustain the long-term enhancement of forest productivity under elevated CO_2. *Ecol. Lett.* **14**, 349–357 (2011).
17. Terrer, C., Vicca, S., Hungate, B. A., Phillips, R. P. & Prentice, I. C. Mycorrhizal association as a primary control of the CO_2 fertilization effect. *Science* **353**, 72–74 (2016).
18. Cox, P. M. et al. Sensitivity of tropical carbon to climate change constrained by carbon dioxide variability. *Nature* **494**, 341–344 (2013).
19. Wenzel, S., Cox, P. M., Eyring, V. & Friedlingstein, P. Projected land photosynthesis constrained by changes in the seasonal cycle of atmospheric CO_2. *Nature* **538**, 499–501 (2016).
20. Mystakidis, S., Davin, E. L., Gruber, N. & Seneviratne, S. I. Constraining future terrestrial carbon cycle projections using observation-based water and carbon flux estimates. *Glob. Change Biol.* **22**, 2198–2215 (2016).
21. Zhao, C. et al. Plausible rice yield losses under future climate warming. *Nat. Plants* **3**, 16202 (2016).
22. Lian, X. et al. Partitioning global land evapotranspiration using CMIP5 models constrained by observations. *Nat. Clim. Change* **8**, 640–646 (2018).
23. Huntzinger, D. N. et al. The North American Carbon Program Multi-scale Synthesis and Terrestrial Model Intercomparison Project - Part 1: overview and experimental design. *Geosci. Model Dev.* **6**, 2121–2133 (2013).
24. Norby, R. J., Warren, J. M., Iversen, C. M., Medlyn, B. E. & McMurtrie, R. E. CO_2 enhancement of forest productivity constrained by limited nitrogen availability. *Proc. Natl. Acad. Sci. USA* **107**, 19368–19373 (2010).
25. De Kauwe, M. G. et al. Where does the carbon go? A model-data intercomparison of vegetation carbon allocation and turnover processes at two temperate forest free-air CO_2 enrichment sites. *New Phytol.* **203**, 883–899 (2014).
26. Franks, P. J. et al. Sensitivity of plants to changing atmospheric CO_2 concentration: from the geological past to the next century. *New Phytol.* **197**, 1077–1094 (2013).
27. Wang, H. et al. Towards a universal model for carbon dioxide uptake by plants. *Nat. Plants* **3**, 734–741 (2017).
28. Bacastow, R. & Keeling, C. D. in *Carbon and the* Biosphere (eds Woodwell, G. M. & Pecan, E. V.) 86–135 (US Dep. of Comm., 1973).
29. Peñuelas, J. et al. Human-induced nitrogen–phosphorus imbalances alter natural and managed ecosystems across the globe. *Nat. Commun.* **4**, 2934 (2013).
30. McCarthy, H. R. et al. Re-assessment of plant carbon dynamics at the Duke free-air CO_2 enrichment site: interactions of atmospheric $[CO_2]$ with nitrogen and water availability over stand development. *New Phytol.* **185**, 514–528 (2010).
31. Reich, P. B. & Hobbie, S. E. Decade-long soil nitrogen constraint on the CO_2 fertilization of plant biomass. *Nat. Clim. Change* **3**, 278–282 (2013).
32. Norby, R. J. et al. Model-data synthesis for the next generation of forest free-air CO_2 enrichment (FACE) experiments. *New Phytol.* **209**, 17–28 (2016).
33. Drake, J. E. et al. Short-term carbon cycling responses of a mature eucalypt woodland to gradual stepwise enrichment of atmospheric CO_2 concentration. *Glob. Change Biol.* **22**, 380–390 (2016).

34. Medlyn, B. E. et al. Using ecosystem experiments to improve vegetation models. *Nat. Clim. Change* **5**, 528–534 (2015).

Acknowledgements

This study was supported by the Strategic Priority Research Program (A) of the Chinese Academy of Sciences (Grant XDA20050101), the National Key R&D Program of China (2017YFA0604702), and the National Natural Science Foundation of China (41861134036, 41701089). The full list of acknowledgements is provided in the Supplementary Information.

Author contributions

S.P., Y.L., T.G. and P.C. designed the study. Y.L. performed the analysis. Y.L. and S.P. drafted the paper. All authors contributed to the interpretation of the results and to the text.

Competing interests

The authors declare no competing interests.

Additional information

Supplementary information is available for this paper at https://doi.org/10.1038/s41561-019-0436-1.

Reprints and permissions information is available at www.nature.com/reprints.

Correspondence and requests for materials should be addressed to S.P.

Methods

Observed site-scale sensitivity of NEP to eCO$_2$ concentration (B_{Site}) from CO$_2$ enrichment experiments. We collected the data at the eCO$_2$ experiments for the effect of eCO$_2$ on NEP from the publications (Supplementary Table 2). Experimental sites with observational periods shorter than one growing season in each measurement year were excluded. A total of seven eCO$_2$ experimental sites were used in our study (Supplementary Table 2). The B_{Site} observed at each site ($B_{\text{Site}}^{\text{Obs}}$) was calculated as:

$$B_{\text{Site}}^{\text{Obs}} = \frac{\Delta\text{NEP}}{\Delta\text{CO}_2} \tag{1}$$

where ΔNEP was calculated as the difference in NEP between the eCO$_2$ and control treatments, and ΔCO$_2$ is the atmospheric CO$_2$ concentrations in the eCO$_2$ treatment minus the control ambient concentration during the experiment; ΔCO$_2$ differs between experiments. For the FACE experiments at Oak Ridge National Laboratory (ORNL-FACE), Duke-FACE, Rhinelander (Aspen-FACE) and Merritt Island, ΔNEP caused by eCO$_2$ was calculated as the eCO$_2$-induced change in ecosystem carbon storage divided by the experimental period.

MsTMIP simulations used to analyse eCO$_2$ impact on terrestrial carbon sink. We used net ecosystem CO$_2$ exchange (NEE, variable 'NEE' in the MsTMIP product) from the simulations of 12 terrestrial carbon-cycle models from the MsTMIP (Supplementary Table 1). The outputs of all models were downloaded from https://doi.org/10.3334/ORNLDAAC/1225 (ref. [35]). Driver data of MsTMIP were downloaded from https://doi.org/10.3334/ORNLDAAC/1220 (ref. [36]). The outputs and driver data cover all land surface areas excluding Antarctica with a 0.5° × 0.5° spatial resolution. The models simulated four sensitivities to test the influence of climate, land-use and land-cover change (LULCC), CO$_2$ concentrations and nitrogen (N) deposition on the terrestrial carbon cycle: (1) the models were forced by time-varying climate (scenario SG1), (2) the models were forced by time-varying climate and LULCC (scenario SG2), (3) the models were forced by time-varying climate, LULCC and CO$_2$ concentration (scenario SG3), and (4) the models with C–N interactions were forced by time-varying climate, LULCC, CO$_2$ concentration and N deposition (scenario BG1). The effect of rising CO$_2$ was isolated as the differences between SG3 and SG2. To analyse eCO$_2$ impact on terrestrial carbon sink, we used a total of 12 models (CLM4, CLM4VIC, DLEM, GTEC, ISAM, LPJ-wsl, ORCHIDEE-LSCE, SiBCASA, TEM6, TRIPLEX-GHG, VEGAS2.1 and VISIT) with both SG2 and SG3 simulations, complying with the following conditions: they provided variables for NEE (variable 'NEE'), NPP (variable 'NPP'), total biomass carbon pool (variable 'TotLivBiom', except 'CarbPools' for TRIPLEX-GHG SG2 simulations) and soil carbon pool (variable 'TotSoilCarb', except 'CarbPools' for CLM4VIC and VISIT), and we could apply the two-box model (see below) for calibrating the outputs. Here, soil carbon pool includes soil carbon and litter carbon.

Calculation of the changes in the global residual terrestrial carbon sink relative to 1959 and its drivers. The residual terrestrial sink (S_{LAND}) in MsTMIP was calculated as the integrated effect of time-varying climate, CO$_2$ concentrations and N deposition on global terrestrial carbon sink (Fig. 1a). The effect of climate change on S_{LAND} was given by the SG1 scenario. The effects of the other forcing factors on S_{LAND} were calculated using differences between the simulations: differences between SG3 and SG2 for the effect of rising CO$_2$ (Fig. 1b and Supplementary Fig. 18) and differences between BG1 and SG3 for the effect of variations in N deposition (Supplementary Fig. 19). The S_{LAND} from Global Carbon Budget (GCB) 2017 (refs. [2,37]) was estimated by subtracting the growth rate in atmospheric CO$_2$ concentration (G_{ATM}) and ocean CO$_2$ sink (S_{OCEAN}) from global emissions from fossil fuels and industry (E_{FF}) and land-use change (E_{LUC}): $S_{\text{LAND}} = \text{E}_{\text{FF}} + \text{E}_{\text{LUC}} - (G_{\text{ATM}} + S_{\text{OCEAN}})$ (Fig. 1a).

Sensitivity of Northern Hemisphere temperate (23–50° N) terrestrial carbon sink to eCO$_2$ (B_{NH}) in MsTMIP. The sensitivity of the Northern Hemisphere temperate terrestrial carbon sink to eCO$_2$ ($B_{\text{NH}}^{\text{Mod}}$) for 1959–2010 was calculated as $B_{\text{NH}}^{\text{Mod}} = \Delta\text{NEP}/\Delta\text{CO}_2$, where ΔNEP is the difference in the CO$_2$-caused Northern Hemisphere temperate terrestrial NEP (variable 'NEE' in the MsTMIP product, SG3-SG2) between 2001–2010 and 1959–1968, and ΔCO$_2$ is the difference in the global atmospheric CO$_2$ concentration between 2001–2010 and 1959–1968.

Sensitivity of the modelled site-scale NEP to eCO$_2$ ($B_{\text{Site}}^{\text{Mod}}$) for the seven eCO$_2$ experimental sites in MsTMIP. We established a two-box model for each model and each site to obtain the effects of short-term pulses of eCO$_2$ on NEP from the MsTMIP models. We then used these two-box models to replicate the eCO$_2$ experiments with the form of changing CO$_2$ identical to that in the eCO$_2$ experiments.

First, we extracted the NPP, total biomass carbon and soil carbon variables of each MsTMIP model for each eCO$_2$ experimental site by averaging the values in the grid cells with the same dominant vegetation type as in the field experiment within a 4.5° × 4.5° window around the eCO$_2$ experimental site. We use a 4.5° × 4.5° window in this study partly because it is the minimum spatial scale for which the same vegetation type that, corresponding to the FACE sites, is represented in all the MsTMIP models. The LULCC data set driving the MsTMIP simulations contained 47 classes of synergetic land-cover MAP (SYNMAP)[38,39]. We reclassified this data set ('biome_frac' variable) into the SIMPLE legend categories defined by Jung et al.[38] to obtain the spatial distributions of the forest and grassland fractions ('Trees' and 'Grasses' in the SIMPLE legend). Grid cells with mean fractions of trees or grasses during 1959–2010 not less than 50% were tagged 'forest' or 'grassland', respectively. Moreover, we analysed the relationship between the climate conditions in the 4.5° × 4.5° window and central 0.5° × 0.5° grid across the seven eCO$_2$ experiment sites (Supplementary Fig. 21). Results show that, as expected, there are large variations in climate conditions (temperature and precipitation) among the seven sites, but for each individual site the climate conditions (temperature and precipitation) in the 4.5° × 4.5° window are very close to those at the central 0.5°×0.5° grid (Supplementary Fig. 21). The 4.5° × 4.5° window also generally captures the spatial variability of soil texture (clay, sand and silt fraction) across the seven eCO$_2$ experiment sites (Supplementary Fig. 22).

Second, we assumed that the total biomass-carbon pool (C_{B}) had a constant rate of decay (μ) and that the soil-carbon pool (C_{S}) also had a constant rate of decay (ρ). The decaying carbon from the total biomass pool (B2S) enters the soil pool, and the decaying carbon from the soil pool is emitted to the atmosphere as HR. This simple system was represented by a linear two-box model:

$$\begin{cases} \frac{\text{d}\Delta C_{\text{B}}}{\text{dt}} = \Delta\text{NPP}(t) - \mu \times \Delta C_{\text{B}}(t) \\ \frac{\text{d}\Delta C_{\text{S}}}{\text{dt}} = \mu \times \Delta C_{\text{B}}(t) - \rho \times \Delta C_{\text{S}}(t) \end{cases} \tag{2}$$

The analytical solution was:

$$\begin{cases} \Delta\text{C}_{\text{B}}(t) = \int_0^{\text{t}} [\exp(-\mu t') \times \Delta\text{NPP}(t - t')]\text{d}t' \\ \Delta\text{B2S}(t) = \mu \times \Delta\text{C}_{\text{B}}(t) \\ \Delta\text{C}_{\text{S}}(t) = \int_0^{\text{t}} [\exp(-\rho t') \times \Delta\text{B2S}(t - t')]\text{d}t' \\ \Delta\text{HR}(t) = \rho \times \Delta\text{C}_{\text{S}}(t) \end{cases} \tag{3}$$

Where ΔNPP(t) is the CO$_2$-induced NPP (SG3 – SG2) in year t, ΔC$_{\text{B}}$(t) is the change in CO$_2$-induced total biomass-carbon storage (SG3 – SG2) in year t relative to the first year, ΔC$_{\text{S}}$(t) is the change in CO$_2$-induced soil-carbon storage (SG3 – SG2) in year t relative to the first year, μ is the constant decay rate of ΔC$_{\text{B}}$ ($0 \leq \mu \leq 1$), ΔB2S(t) is the carbon flux from ΔC$_{\text{B}}$ to ΔC$_{\text{S}}$ in year t, ρ is the constant decay rate of ΔC$_{\text{S}}$ ($0 \leq \rho \leq 1$), ΔHR(t) is the CO$_2$-induced heterotrophic respiration in year t.

The parameters μ and ρ for each eCO$_2$ experimental site in each model were fitted with equation (3) using NPP, total biomass-carbon pool and soil-carbon pool for 1901–2010 from the MsTMIP outputs using Matlab (R2018a) software. The codes are shown in Supplementary Information. The two-box models generally emulated successfully the eCO$_2$-induced historical biomass and soil carbon evolution at the seven eCO$_2$ sites from the original complex process-oriented MsTMIP models (Supplementary Figs. 2–13). Nevertheless, the substitute models do not work well at reproducing the biomass-carbon pool evolution at grassland sites for 5 of 12 MsTMIP models (CLM4, GTEC, LPJ-wsl, ORCHIDEE-LSCE and SiBCASA at Duolun, and CLM4, LPJ-wsl and SiBCASA models at PHACE). This model underperformance is particularly when net primary productivity monotonically increases but biomass-carbon pool suddenly declines (Supplementary Figs. 2, 5, 7–9).

Third, we reproduced the eCO$_2$ experiment using the two-box model for each eCO$_2$ experimental site in each MsTMIP model, assuming that CO$_2$ abruptly increased by 60 ppm (from 320 ppm to 380 ppm) and was then held fixed. This analysis was performed with the following steps. (1) Calculate eCO$_2$-induced NPP in the reproduced eCO$_2$ experiment ($\Delta\text{NPP}^{\text{site\_FACE\_M}}$). We assumed that $\Delta\text{NPP}^{\text{site\_FACE\_M}}$ was a constant and the same as the long-term response of NPP to eCO$_2$ in the MsTMIP simulations. Therefore, $\Delta\text{NPP}^{\text{site\_FACE\_M}} = \frac{\Delta\text{NPP}}{\Delta\text{CO}_2} \times 60$, where ΔNPP is the modelled difference in CO$_2$-induced NPP in the same months as the corresponding eCO$_2$ experiment between 2001–2010 and 1959–1968 and ΔCO$_2$ is the difference in the atmospheric CO$_2$ concentration between 2001–2010 and 1959–1968. (2) Calculate eCO$_2$-induced HR in the reproduced eCO$_2$ experiment ($\Delta\text{HR}^{\text{site\_FACE\_M}}$). We calculated $\Delta\text{HR}^{\text{site\_FACE\_M}}$ using equation (3) for each MsTMIP model on the basis of its fitted parameters (μ and ρ) and $\Delta\text{NPP}^{\text{site\_FACE\_M}}$. (3) Calculate eCO$_2$-induced NEP in the reproduced FACE experiment ($\Delta\text{NEP}^{\text{site\_FACE\_M}}$) as $\Delta\text{NEP}^{\text{site\_FACE\_M}} = \Delta\text{NPP}^{\text{site\_FACE\_M}} - \Delta\text{HR}^{\text{site\_FACE\_M}}$. (4) Calculate the sensitivity of NEP to eCO$_2$ in the reproduced eCO$_2$ experiment ($B_{\text{Site}}^{\text{Mod}}$) as $B_{\text{Site}}^{\text{Mod}} = \Delta\text{NEP}^{\text{site\_FACE\_M}}/60$ (Supplementary Fig. 1). (5) When comparing with FACE observations, the duration for the calculation of $B_{\text{Site}}^{\text{Mod}}$ is site specific and is the same as the duration in the real FACE experiment at each site. For example, the duration of Duke-FACE is nine years, from 1997 to 2005 (Supplementary Table 2). The $B_{\text{Site}}^{\text{Mod}}$ was calculated as the mean of $B_{\text{Site}}^{\text{Mod}}$ in the nine years from the first to the ninth experimental years in the two-box-model-based FACE experiment at Duke-FACE site (Supplementary Fig. 16). The simulated B_{Site} in Fig. 2a,c,e is the mean $B_{\text{Site}}^{\text{Mod}}$ for the seven eCO$_2$ sites for each model.

Transform observed site-scale NEP sensitivity to elevated atmospheric CO_2 in eCO_2 experiments (B_{Site}^{Obs}) to the NEP sensitivity at a lower CO_2 concentration level (B_{Site}^{Hist}). In the eCO_2 experiments, atmospheric CO_2 concentration (c_a) was increased from ambient (average ~381 ppm) to a very high concentration roughly representative of two times pre-industrial values (average ~588 ppm, indicated as ≈ 2×CO_2). This change in c_a is much larger than that used in MsTMIP model simulations (from ~320 ppm during 1959–1968 to ~380 ppm during 2001–2010). To convert NEP responses at ≈ 2×CO_2 c_a in eCO_2 experiments to responses at historical c_a values, for each eCO_2 experiment, we extrapolated the observed NEP sensitivity with CO_2 increasing from control c_a (c_{a2}) to treatment c_a (c_{a2p}) to the NEP sensitivity with CO_2 increasing from 320 ppm (c_{a1}) to 380 ppm (c_{a1p}).

Assuming that carbon use efficiency (CUE = NPP/GPP) and turnover rates of carbon pools in short-term eCO_2 experiments are unchanged when CO_2 varies from c_{a1} to c_{a1p} compared to from c_{a2} to c_{a2p} (Supplementary Figs. 23 and 24), eCO_2-induced NEP changes proportionally with eCO_2-induced GPP according to Supplementary equation (5), equivalent to the following equation:

$$\frac{B_{NEP1}}{B_{NEP2}} = \frac{B_{GPP1}}{B_{GPP2}} \tag{4}$$

where B_{NEP1} and B_{GPP1} are the CO_2 fertilization effects on NEP and GPP over c_a ranging from c_{a1} to c_{a1p} and B_{NEP2} and B_{GPP2} are the CO_2 fertilization effects on NEP and GPP over c_a ranging from c_{a2} to c_{a2p}.

The response of GPP to rising c_a can be estimated with a first-principles-based universal model of photosynthesis (Pmodel), which is extensively supported by flux observations and FACE experiment[27]. The form of Pmodel is a 'light-use efficiency' (LUE) model that predicted GPP is proportional to absorbed photosynthetically active radiation (PAR), where the LUE is predicted from first principles[27]. The standard biochemical model of photosynthesis proposed by Farquhar et al.[40] predicts the instantaneous rates of photosynthesis limited by Rubisco (A_c) and electron-transport (A_J), respectively. The coordination or colimitation hypothesis states that the maximum capacity of carboxylation acclimates to the prevailing environmental conditions at weekly or longer time scales, allowing the two photosynthetic processes of A_c and A_J to be coordinated with each other ($A_J = A_c$) under typical daytime conditions[27,41,42]. The LUE model descriptions are in the methods of ref. [27] and more detailed information can be found in section 5 of "A light-use efficiency model for GPP" in the supplementary information. The calculation of GPP is shown as following equations (5) and (6) (equations [2] and [3] in ref. [27]).

$$\mathrm{GPP} = \varphi_0 I_{abs} m \sqrt{\left[1-(c^\star/m)^{2/3}\right]} \tag{5}$$

where

$$\mathrm{m} = (c_a - \Gamma^\star)/\left\{c_a + 2\Gamma^\star + 3\Gamma^\star\sqrt{\left[1.6\eta^\star D_0 \beta^{-1}(K+\Gamma^\star)^{-1}\right]}\right\} \tag{6}$$

Here, c_a is atmospheric CO_2 concentration (ppm), φ_0 is the intrinsic quantum yield ($\mathrm{g\,C\,mol^{-1}}$), m is a component of light-use efficiency, I_{abs} is the absorbed photosynthetic photon flux density ($\mathrm{mol\,m^{-2}\,s^{-1}}$), $\Gamma^\star$ is the photorespiratory compensation point (Pa), K is the effective Michaelis–Menten coefficient of Rubisco (Pa), $\eta^\star$ is the viscosity of water relative to its value at 25 °C, D_0 is vapour pressure deficit (Pa), and $c^\star$ and β represent the cost factor of the maintaining electron transport capacity (~0.41) and the ratio of carboxylation to transpiration cost factors (~240). Both are estimated from independent observational data.

According to this model, the ratio between GPP sensitivities to elevated CO_2 from c_{a1} to c_{a1p} and from c_{a2} to c_{a2p} (Supplementary Fig. 25) is estimated as:

$$\frac{\mathrm{B_{GPP1}}}{\mathrm{B_{GPP2}}} = \frac{m_{1p}\sqrt{\left[1-(c^\star/m_{1p})^{2/3}\right]} - m_1\sqrt{\left[1-(c^\star/m_1)^{2/3}\right]}}{m_{2p}\sqrt{\left[1-(c^\star/m_{2p})^{2/3}\right]} - m_2\sqrt{\left[1-(c^\star/m_2)^{2/3}\right]}} \times \frac{(c_{a2p}-c_{a2})}{(c_{a1p}-c_{a1})} \tag{7}$$

Here, m_1, m_{1p}, m_2 and m_{2p} are m calculated at c_{a1}, c_{a1p}, c_{a2} and c_{a2p}, respectively, using equation (6). We estimated m from growing-season mean temperature (tmp), diurnal temperature range (dtr), relative humidity (reh) and elevation (elv) extracted from CRU climatology (CRU CL v. 2.0) at 10-minute resolution[43].

The observed NEP sensitivity measured at ≈ 2×CO_2 in eCO_2 experiments (B_{Site}^{Obs}) was extrapolated to the sensitivity at CO_2 ranging from 320 to 380 ppm in the simulations (B_{Site}^{Hist}):

$$B_{Site}^{Hist} = B_{Site}^{Obs} \times \frac{B_{GPP1}}{B_{GPP2}} \tag{8}$$

PDF of B_{Site}^{Hist} from eCO_2 experiments. The average B_{Site}^{Hist} from the eCO_2 experiments and its uncertainty were estimated using a bootstrap approach with the following steps. (1) One B_{Site}^{Hist} was randomly drawn for each eCO_2 experiment site (see experimental data in Supplementary Table 2), and the selected B_{Site}^{Hist} from all eCO_2 experiment sites were then averaged to obtain B_{Site}^{Hist}. (2) Step (1) was performed 1,000 times to obtain 1,000 B_{Site}^{Hist}. (3) The mean and standard deviation of the 1,000 B_{Site}^{Hist} from step (2) were calculated to obtain mean B_{Site}^{Hist} ($\overline{B_{Site}^{Hist}}$) and its uncertainty [$\sigma\left(B_{Site}^{Hist}\right)$] from the eCO_2 experiments. This uncertainty represented the site-scale uncertainty due to experimental procedures, such as uneven measurements and sample time, rather than to spatial heterogeneity across sites. The uncertainty could therefore be comparable to the mean of simulated B_{Site} (B_{Site}^{Mod}) for the seven eCO_2 experiment sites for each model (Fig. 2a,c,e). We assumed that all observations could be represented by a Gaussian distribution, with mean and standard deviation obtained using this bootstrap approach.

Least-squares linear regression between B_{NH}^{Mod} and B_{Site}^{Mod} across the MsTMIP models. This study used an emergent-constraint approach proposed by Cox et al.[18]. We identified a linear least-squares regression between B_{NH}^{Mod} and B_{Site}^{Mod} across the MsTMIP models:

$$B_{NH}^{Mod}(i) = \mathrm{a} \times B_{Site}^{Mod}(i) + b \tag{9}$$

where $B_{NH}^{Mod}(i)$ is B_{NH}^{Mod} of model i, and $B_{Site}^{Mod}(i)$ is B_{Site}^{Mod} of model i.

The least-squares error of the regression model was calculated as:

$$s^2 = \frac{1}{N-2}\sum_{i=1}^{N}\left[B_{NH}^{Mod}(i) - \tilde{B}_{NH}^{Mod}(i)\right]^2 \tag{10}$$

where N is the number of models used in the regression model, $B_{NH}^{Mod}(i)$ is B_{NH}^{Mod} of model i, and $\tilde{B}_{NH}^{Mod}(i)$ is the predicted B_{NH}^{Mod} using the regression model at B_{Site}^{Mod} of model i.

The 'prediction error' of $\tilde{B}_{NH}^{Mod}$ based on the regression model for a given x was:

$$\sigma\left(\tilde{B}_{NH}^{Mod}|x\right) = s\sqrt{1 + \frac{1}{N} + \frac{(x-\bar{x})^2}{N\sigma_x^2}} \tag{11}$$

where $\bar{x}$ is the mean of $x_1, x_2 \ldots x_N$ and σ_x is the standard deviation of $x_1, x_2 \ldots x_N$.

The probability density of B_{NH}^{Mod} for a given x was:

$$P_{reg}\left(B_{NH}^{Mod}|x\right) = \frac{1}{\sqrt{2\pi\sigma\left(\tilde{B}_{NH}^{Mod}|x\right)^2}} e^{-\frac{\left[B_{NH}^{Mod} - \left(\tilde{B}_{NH}^{Mod}|x\right)\right]^2}{2\sigma\left(\tilde{B}_{NH}^{Mod}|x\right)^2}} \tag{12}$$

Constraint on B_{NH}. The PDF for B_{NH} derived from observations ($\mathrm{B}_{NH}^{Constrained}$), the red lines in Fig. 2b,d,f, were calculated as:

$$P\left(\mathrm{B}_{NH}^{Constrained}\right) = \int_{-\infty}^{+\infty} P_{reg}\left(\mathrm{B}_{NH}^{Mod}|x\right) \times \frac{1}{\sqrt{2\pi\sigma\left(\mathrm{B}_{Site}^{Hist}\right)^2}} e^{-\frac{\left(x-\overline{\mathrm{B}_{Site}^{Hist}}\right)^2}{2\sigma\left(\mathrm{B}_{Site}^{Hist}\right)^2}} \mathrm{d}x \tag{13}$$

Analysis of the robustness of $B_{NH}^{Constrained}$ when using fewer than seven eCO_2 experiment sites. We performed the following steps. (1) We randomly selected N eCO_2 experiment sites to calculate the constrained B_{NH} using all 12 models. (2) Step (1) was performed 1,000 times to obtain 1,000 constrained B_{NH}. (3) All constrained B_{NH} in step (2) were averaged to obtain the mean constrained B_{NH}. We took N = 6, 5 and 4 (Supplementary Fig. 14).

Analysis of the robustness of $B_{NH}^{Constrained}$ when using a logarithmic function. The responses of GPP to rising c_a can be estimated with a logarithmic function (equation 15 in ref. [3]) that was first introduced by Bacastow et al.[28]:

$$P_t = P_0\left[1 + \mathrm{B_{log}}\ln\left(\frac{C_t}{C_0}\right)\right] \tag{14}$$

Here, P_t and P_0 are ecosystem carbon fluxes (GPP, NPP or NEP) for c_t and c_0 CO_2 concentration, B_{log} is a constant factor. Thus, B_{GPP1}/B_{GPP2} in equation (8) is expressed in this case as:

$$\begin{aligned}\frac{\mathrm{B_{GPP1}}}{\mathrm{B_{GPP2}}} &= \frac{\left\{GPP_0\left[1+\mathrm{B_{log}}\ln(c_{a1p}/c_{a0})\right] - GPP_0\left[1+\mathrm{B_{log}}\ln(c_{a1}/c_{a0})\right]\right\}/(c_{a1p}-c_{a1})}{\left\{GPP_0\left[1+\mathrm{B_{log}}\ln(c_{a2p}/c_{a0})\right] - GPP_0\left[1+\mathrm{B_{log}}\ln(c_{a2}/c_{a0})\right]\right\}/(c_{a2p}-c_{a2})} \\ &= \frac{\left[\ln(c_{a1p}) - \ln(c_{a1})\right]/(c_{a1p}-c_{a1})}{\left[\ln(c_{a2p}) - \ln(c_{a2})\right]/(c_{a2p}-c_{a2})}\end{aligned} \tag{15}$$

We analysed the emergent constraints on the sensitivity of the Northern Hemisphere terrestrial carbon sink to elevated atmospheric CO_2 concentration using equation (15), rather than equation (7), with the other conditions unchanged (Supplementary Fig. 15).

Constraining the sensitivity of global terrestrial carbon sink to eCO_2. Using all 12 MsTMIP models and the observations at the seven eCO_2 experiment sites, we analysed the constrained sensitivity of global terrestrial carbon sink to eCO$_2$ during 1959–2010 ($B_{\mathrm{Globe}}^{\mathrm{Constrained}}$). The approach was the same as for the calculation of $B_{\mathrm{NH}}^{\mathrm{Constrained}}$ but using the sensitivity of global terrestrial carbon sink to eCO$_2$ (B_{Globe}) (Supplementary Fig. 17).

Constraining the sensitivity of global terrestrial carbon sink to long-term climate change (Γ_{Long}). We identified an emergent relationship between Γ_{Long} and the sensitivity of global terrestrial carbon sink to interannual variability in climate (Γ_{IAV}) across 13 MsTMIP models (BIOME-BGC, CLM4, CLM4VIC, DLEM, GTEC, ISAM, LPJ-wsl, ORCHIDEE-LSCE, SiB3, SiBCASA, TEM6, VEGAS2.1 and VISIT) with SG1 and SG3/BG1 (SG3 for carbon-only models and BG1 for C–N models) outputs (Supplementary Fig. 20), similar to Huntzinger et al.[6] but focusing on the Γ_{Long} during 1959–2010. CLASS-CTEM-N was not used following Ito et al.[44] because its net CO$_2$ exchange was always negative. TRIPLEX-GHG was not used because SG1 simulation is not available from https://doi.org/10.3334/ORNLDAAC/1225 (ref. [35]).

Γ_{Long} and Γ_{IAV} were calculated using the approach from Huntzinger et al.[6]. Γ_{Long} was calculated by regressing the land annual NEE given by the SG1 scenario against temperature and precipitation during 1959–2010 from the MsTMIP driver data set. The regression coefficient on temperature was used to determine Γ_{Long}. Γ_{IAV} was calculated by regressing the detrended land annual NEE given by the SG3 (for carbon-only models) or BG1 (for C–N models) scenario against detrended temperature during 1959–2010 from the MsTMIP driver data set. The detrended NEE and the detrended temperature were calculated by subtracting 11-year running means. The 11-year running means were calculated using 'runmean' function (https://www.mathworks.com/matlabcentral/fileexchange/10113-runmean, last accessed June 25, 2018) with its parameters 'M' and 'MODESTR' set as '5' and 'edge', respectively. The post-volcano years (1963, 1964, 1982, 1983, 1991 and 1992) were removed before calculating both Γ_{Long} and Γ_{IAV}.

The Γ_{IAV} from GCB 2017 (refs. [2,37]) was used as an observational constraint on the Γ_{Long} (Supplementary Fig. 20). The GCB Γ_{IAV} was calculated by regressing the detrended GCB net land sink (NLS) against detrended temperature from the MsTMIP driver data set, using the same approach as the calculation of Γ_{IAV} in MsTMIP models. The GCB NLS was estimated by subtracting the growth rate in atmospheric CO$_2$ concentration and ocean CO$_2$ sink from global emissions from fossil fuels and industry: $\mathrm{NLS} = \mathrm{E_{FF}} - \mathrm{G_{ATM}} - \mathrm{S_{OCEAN}}$. The GCB Γ_{IAV} is estimated as $-2.36 \pm 0.77\,\mathrm{PgC\,yr^{-1}\,K^{-1}}$ (mean ± 1 standard error). Using this as an observational constraint, the constrained Γ_{Long} is estimated as $-1.57 \pm 0.51\,\mathrm{PgC\,yr^{-1}\,K^{-1}}$ on the basis of the linear relationship between Γ_{Long} and Γ_{IAV} across MsTMIP models (Supplementary Fig. 20).

Data availability

Driver data of MsTMIP models are available from https://doi.org/10.3334/ORNLDAAC/1220. The outputs of MsTMIP models are available from https://doi.org/10.3334/ORNLDAAC/1225. Global Carbon Budget 2017 data (Global_Carbon_Budget_2017v1.3.xlsx) are available from https://doi.org/10.18160/GCP-2017. CRU climatology data (CRU CL v. 2.0) are available from https://crudata.uea.ac.uk/cru/data/hrg/.

Code availability

The code for fitting the two-box model, as given in equation (3), is shown in Supplementary Information.

References

35. Huntzinger, D. N. et al. NACP MsTMIP: Global 0.5-deg Terrestrial Biosphere Model Outputs (version 1) in Standard Format. *ORNL DAAC* https://doi.org/10.3334/ORNLDAAC/1225 (2016).
36. Wei, Y. et al. NACP MsTMIP: Global and North American Driver Data for Multi-model Intercomparison. *ORNL DAAC* https://doi.org/10.3334/ORNLDAAC/1220 (2014).
37. Supplemental data of Global Carbon Budget 2017 (Version 1.0). *Global Carbon Project* https://doi.org/10.18160/gcp-2017 (2017).
38. Jung, M., Henkel, K., Herold, M. & Churkina, G. Exploiting synergies of global land cover products for carbon cycle modeling. *Remote Sens. Environ.* **101**, 534–553 (2006).
39. Wei, Y. et al. The North American Carbon Program Multi-scale Synthesis and Terrestrial Model Intercomparison Project: part 2: environmental driver data. *Geosci. Model Dev.* **7**, 2875–2893 (2014).
40. Farquhar, G. D., Caemmerer, S. V. & Berry, J. A. A biochemical model of photosynthetic CO$_2$ assimilation in leaves of C$_3$ species. *Planta* **149**, 78–90 (1980).
41. Maire, V. et al. The coordination of leaf photosynthesis links C and N fluxes in C$_3$ plant species. *PLoS ONE* **7**, e38345 (2012).
42. Togashi, H. F. et al. Thermal acclimation of leaf photosynthetic traits in an evergreen woodland, consistent with the coordination hypothesis. *Biogeosciences* **15**, 3461–3474 (2018).
43. Mark, N., David, L., Mike, H. & Ian, M. A high-resolution data set of surface climate over global land areas. *Clim. Res.* **21**, 1–25 (2002).
44. Ito, A. et al. Decadal trends in the seasonal-cycle amplitude of terrestrial CO$_2$ exchange resulting from the ensemble of terrestrial biosphere models. *Tellus B Chem. Phys. Meteor.* **68**, 28968 (2016).